Research Article

Spatiotemporal High-Resolution Cloud Mapping with a Ground-Based IR Scanner

Benjamin Brede,[1] Boris Thies,[2] Jörg Bendix,[2] and Uwe Feister[3]

[1]*Laboratory of Geo-Information Science and Remote Sensing, Wageningen University and Research Centre,*
 Droevendaalsesteeg 3, 6708 PB Wageningen, Netherlands
[2]*Laboratory for Climatology and Remote Sensing, Faculty of Geography, University of Marburg, Deutschhausstr. 10,*
 35032 Marburg, Germany
[3]*Meteorological Observatory Lindenberg-Richard-Aßmann-Observatory, German Meteorological Service, Lindenberg, Germany*

Correspondence should be addressed to Benjamin Brede; benjamin.brede@wur.nl

The high spatiotemporal variability of clouds requires automated monitoring systems. This study presents a retrieval algorithm that evaluates observations of a hemispherically scanning thermal infrared radiometer, the NubiScope, to produce georeferenced, spatially explicit cloud maps. The algorithm uses atmospheric temperature and moisture profiles and an atmospheric radiative transfer code to differentiate between cloudy and cloudless measurements. In case of a cloud, it estimates its position by using the temperature profile and viewing geometry. The proposed algorithm was tested with 25 cloud maps generated by the Fmask algorithm from Landsat 7 images. The overall cloud detection rate was ranging from 0.607 for zenith angles of 0 to 10° to 0.298 for 50–60° on a pixel basis. The overall detection of cloudless pixels was 0.987 for zenith angles of 30–40° and much more stable over the whole range of zenith angles compared to cloud detection. This proves the algorithm's capability in detecting clouds, but even better cloudless areas. Cloud-base height was best estimated up to a height of 4000 m compared to ceilometer base heights but showed large deviation above that level. This study shows the potential of the NubiScope system to produce high spatial and temporal resolution cloud maps. Future development is needed for a more accurate determination of cloud height with thermal infrared measurements.

1. Introduction

Clouds are of vital importance for the Earth's radiation and energy budget. Their macrophysical structure and their microphysical properties determine their radiative forcing and thus their role within the Earth's climate system. However, they remain one of the largest sources for uncertainties in the global energy budget [1]. The high spatiotemporal variability of clouds which results from their dependence on atmospheric dynamics, water vapour and aerosols, requires operational measurement systems that provide area-wide information about their macro- and microphysical properties. While, on the regional to global scale, satellite-based retrievals to retrieve cloud distribution, cloud properties, and even rainfall are well developed [2, 3], ground-based spatiotemporal observations are hardly available due to a lack of suitable instrumentation. However, retrieving cloudiness on the local scale is of high importance for several fields, including irradiance calculations required for solar power production [4], aviation, and local microclimatological studies.

Ground-based scanners providing data in high spatial and temporal resolution might potentially provide high-resolution information on clouds. However, there are only few commercial instruments available which provide spatiotemporal data on cloudiness for local applications. The Total Sky Imager Model TSI-880 (Yankee Environmental Systems, Inc.) based on an optical camera system is a potentially suitable system which is, however, limited to daytime sky conditions. Available Day-and-Night Imagers such as the Day/Night Whole Sky Imager of the University of California [5] and the infrared cloud imager [6] are not yet commercially available. An IR system commercially available is the NubiScope (IMK/Sattler-SES) [7]. Based on two Heitronics

KT15.82 IIP pyrometers (8–14 μm) the NubiScope scans the sky in 36 azimuth angle steps of 10° and 30 zenith angle steps of 3° with a field of view angle of 3°. Software supplied by the manufacturer translates the raw data into average cloud-base height and cloud cover in three height layers [8, 9]. Since the NubiScope operates fully automated and the algorithm does not require any external input data, cloud cover and cloud-base height information can be obtained 24 hours a day.

The potential of the NubiScope for total cloud cover detection was verified in a number of studies. Boers et al. used the NubiScope together with other remote sensing systems to derive a fractional cloudiness time series at the Cabauw Experimental Site for Atmospheric Research, Netherlands [10]. They concluded that the NubiScope performs well for determination of total cloud cover and propose using NubiScope in combination with a scanning ceilometer for future operational cloud-base determination. Feister et al. compared the performance of the NubiScope cloud cover and cloud-base height products with a Daylight VIS/NIR Whole Sky Imager (WSI), a Vaisala ceilometer LD-40, and a Ka-band cloud radar [11]. They found that in 90% of cases the WSI and the NubiScope cloud cover differences were less than 2 okta. The cloud-base height of the NubiScope showed good correlation with that of the ceilometer up to a height of 3 km. Above 3 km the differences were more random. Wauben tested the NubiScope's performance for 2 months at the Royal Netherlands Meteorological Institute (KNMI) at De Bilt, Netherlands [8]. The agreement with cloud cover from ceilometer time series was good in most of the cases. However, mean NubiScope cloud-base heights were higher than those of the ceilometer. Wauben explains this with partial and semitransparent clouds, which lower the detected brightness temperature and thus increase derived cloud-base height [8]. In contrast to Wauben, Feister et al. found that the mean ceilometer cloud base was higher than the NubiScope cloud base [11]. This on the other hand could be due to unaccounted emission from the atmosphere below the clouds.

Since cloud height is derived by assuming a standard temperature profile, uncertainties in the actual temperature profile make the cloud-base height determination of the NubiScope rather uncertain. Furthermore, there is the effect of water vapour in the 8–14 μm region that leads to increased cloudless sky temperature and thus underestimates cloud-base height with increasing zenith angle. In this context, Feister et al. suggested an improvement of the NubiScope algorithm by including realistic vertical temperature and water vapour distributions from measured or modelled external profiles [11].

In the standard operational mode, the NubiScope provides only an average of cloud cover and cloud-base height over the whole scanned hemisphere. Up to now, the instrument has not been used to produce spatially explicit cloud-base height maps. These are however of valuable benefit since they provide local information in a high spatial and temporal resolution. By combining cloud-base height information derived from the IR temperature detected by the NubiScope together with the corresponding zenith and azimuth angle information, a localization of the detected cloud for every scanned angle combination should be possible. Therefore, the aim of this study is to explore the potential to produce georeferenced spatially explicit cloud-base height maps from NubiScope measurements. The article is structured as follows. Section 2 provides information about data and methods used in this study. This includes the measured temperature and water vapour profiles to improve cloud-base height calculation and the description of the algorithm to determine the cloud localization above the ground. In Section 3, results of the proposed algorithm are presented and compared to satellite images for an evaluation.

2. Data and Methods

2.1. Data

2.1.1. IR Scanner. The instrument used in this study is a version of the NubiScope with two pyrometers. The second pyrometer performs measurements in the opposite direction of the first and thereby halves the scanning time in comparison to the earlier version with one pyrometer. It was installed in December 2009 at the radiation measurement platform atop the laboratory building of the Meteorological Observatory Lindenberg- Richard-Aßmann-Observatory of the German Meteorological Service (DWD) (MOL-RAO, cf. Feister et al., 2010) at 52.2086°N, 14.1213°E, and 127 m asl. The NubiScope scans the sky in 36 azimuth angle steps of 10° and 30 zenith angle steps of 3° with a field of view of 3°. In the present paper, a unique combination of azimuth and zenith angle is called a sterical pixel. One full hemispherical scan takes about 3.5 minutes and starts every 5 minutes. In the manufacturer's algorithm the cloud-base height is calculated by assuming a dry adiabatic lapse rate of 0.98°C per 100 m in the mixing layer, which is fixed to 150 m. Above the mixing layer, a lapse rate of 0.65°C per 100 m for the free atmosphere is used, which is adjusted to the ambient temperature measured by the NubiScope at the horizon. The distinction between low, medium, and high clouds is made by comparing the measured cloud temperature with the lower boundaries for medium and high clouds at 2100 and 5400 m, respectively. For this study, raw data from the period January 2010 to October 2011 were used. Raw data include measured brightness temperatures from all measured zenith-azimuth-combinations and NubiScope internal housing temperature. For technical features of the NubiScope the reader may refer to Table 1.

2.1.2. Temperature, Water Vapour, and Pressure Profiles. To consider the effect of water vapour emission on the NubiScope temperature measurements, temperature and water vapour profiles from a microwave profiler were used in combination with a radiative transfer code. The microwave profiler MP-3001 (Radiometrics Corporation, Boulder, CO, USA) has been operated since 1998 at the MOL [12]. Temperature was given in °C and humidity as absolute humidity in $g\,m^{-3}$ at 47 elevation levels from 112 to 10112 m every 10 minutes. The underlying principles to retrieve temperature and water vapour profiles by means of microwave profilers are described comprehensively elsewhere [13–15]. To

TABLE 1: Technical characteristics of the NubiScope [8].

Characteristics pyrometer	
Spectral range	8 to 14 μm
Temperature range	−100 to 50°C
Temperature accuracy	±0.5°C + 0.7% of target and housing temperature difference
Repeatability	±0.1°C + 0.1%
Response time	300 ms
Characteristics pan-tilt-unit	
Azimuth scan angles	10 to 360°, step 10°
Zenith scan angles	1.5 to 88.5°, step 3°
Accuracy	±0.1°
Operating temperatures	−20 to 60°C (with heating: −40 to 60°C)

obtain pressure profiles data from a Vaisala RS92 radiosonde launched daily at the MOL at 00:00, 06:00, 12:00, and 18:00 UTC was used.

2.1.3. Satellite Images. For validation of the calculated cloud positions from NubiScope measurements, time-synchronous cloud masks derived from Enhanced Thematic Mapper Plus (ETM+) scenes of the Landsat 7 satellite with a spatial resolution of 30 m were used. The cloud masks were derived with the Fmask (Function of mask) algorithm. Fmask is an object-based cloud detection method which makes use of reflectance and brightness temperatures measured with optical and thermal infrared bands [16]. In a validation approach, Fmask reached an overall accuracy of 96.4% for cloud identification compared to manual, visual classification when applied on globally distributed sample scenes [16]. Fmask proved a reliable cloud recognition algorithm and was adopted in the Landsat Climate Data record archive of the US Geological Survey (http://landsat.usgs.gov/CDR_ECV.php), where the sample scenes used in this study were taken from. Table 2 lists the Landsat scenes employed in this study. They represent all scenes for which a coincident NubiScope scan was available during the study period. All scenes were recorded at approximately 9:50 UTC, the time of overpass of Landsat 7 over the Lindenberg Observatory. Therefore, even though the NubiScope is also capable of night-time observations, all validation samples were taken during daytime.

2.1.4. Ceilometer Observations. Simultaneous with the NubiScope observations, ceilometer observations are routinely carried out at the Lindenberg Observatory. For this study we used the CHM 15 k "Nimbus" (Jenoptik, Jena, Germany). This ceilometer can record up to 5 cloud layers, but for this study only the lowest registered layer was considered.

2.2. Cloud-Base Height Mapping Algorithm. In the following sections, the proposed algorithm for spatiotemporal cloud mapping by means of the NubiScope is introduced (cf. Figure 1). In a first step, the algorithm detects cloudy sterical pixels. For this purpose, an atmospheric radiative transfer code is applied. Clouds usually emit more IR radiation than the cloudless sky background. Thus, if the measured brightness temperature exceeds the one for cloudless sky,

TABLE 2: Landsat 7 ETM+ scenes used for validation.

Date	Path/row
13 April 2010	192/24
20 April 2010	193/24
16 June 2010	192/24
23 June 2010	193/24
2 July 2010	192/24
9 July 2010	193/24
10 August 2010	193/24
19 August 2010	192/24
11 September 2010	193/24
7 April 2011	193/24
16 April 2011	192/24
23 April 2011	193/24
3 June 2011	192/24
10 June 2011	193/24
19 June 2011	192/24
5 July 2011	192/24
6 August 2011	192/24
29 August 2011	193/24
14 September 2011	193/24
23 September 2011	192/24
30 September 2011	193/24
9 October 2011	192/24
16 October 2011	193/24

which is simulated with the radiative transfer code, the sterical pixel is treated as cloudy. In this case, its base height is determined by means of an atmospheric temperature profile. From the cloud-base height and the known viewing geometry, the cloud's coordinates at the ground are inferred. Each sterical pixel is treated individually, and the results are combined to produce the final cloud map of a full-scan interval.

2.2.1. Detection of Cloudy Sterical Pixels. Cloud detection is based on the approach of Thurairajah and Shaw [17]. They measured radiance in the 8–14 μm region with an infrared cloud imager and compared the results with modelled radiance based on water vapour measurements from
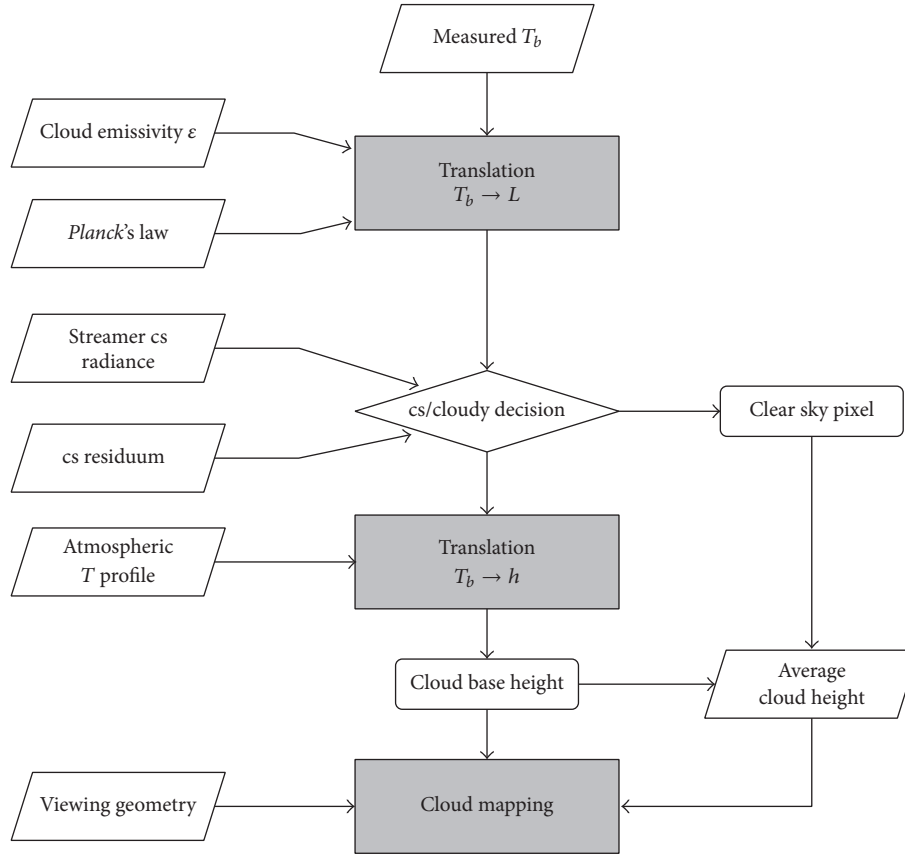
FIGURE 1: Flowchart of the cloud-base height determination for one single sterical pixel (T_b = brightness temperature, L = spectral radiance, cs = cloudless sky, h = cloud-base height, and z = zenith angle) (see text for details).

a microwave radiometer and air temperature. Under cloudless sky conditions, the difference between measured and simulated radiation is theoretically 0. For cloudy conditions, measured radiance is larger than the modelled cloudless sky radiance, due to the higher emission from the cloud base. After subtracting the measured radiance from the modelled radiance for cloudless sky conditions, they obtained residual radiance of $<2\,\mathrm{W\,m^{-2}\,sr^{-1}}$. This difference most likely stems from noise in the electronics as well as from inaccuracies in the retrieval of atmospheric conditions and the resulting error in calculated radiance. Hence, they introduced a threshold below which the difference is still treated as cloudless sky. These thresholds were 1.5 and $2.65\,\mathrm{W\,m^{-2}\,sr^{-1}}$ for their test sites in Barrow and Oklahoma, respectively.

In the present study, the radiative transfer code Streamer [18] was used to model cloudless sky spectral radiance. For each NubiScope scan, a Streamer input file was prepared and the resulting cloudless sky downward radiance in the Streamer bands according to the spectral range of NubiScope was calculated. The required input included the atmospheric profiles derived from the microwave profiler and radiosonde measurements. If the microwave and radiosonde profiles did not temporally match the NubiScope scans, they were temporally interpolated. Radiosonde pressure profiles were interpolated to match the microwave profiler levels. Air temperature, water vapour, and pressure profiles were extended with midlatitude standard profiles to 100 km above ground level. Ozone standard profiles implemented in the code are used. All standard profiles are based on the data of Ellingson et al. [19]. The viewing zenith angle was varied from 1.5° to 85.5° in 3° steps. To compare the simulated spectral radiance with the measured NubiScope brightness temperatures, the latter were translated into spectral radiance B according to Planck's law (see (1)) with an assumed emissivity of 1:

$$B_\lambda\,(T) = \frac{2hc^2}{\lambda^5}\frac{1}{e^{hc/\lambda k_b T} - 1}, \tag{1}$$

where B_λ is spectral radiance, λ is wavelength, T is temperature, h is Planck's constant, c is speed of light, and k_b is Boltzmann's constant.

The simulated radiance for a zenith angle of 3° for 882 scan cycles, identified as cloudless sky by weather observers at MOL, was on average $2.77\,\mathrm{Wm^{-2}\,sr^{-1}}$ smaller than the measured radiance. A positive relationship of the cloudless sky residuals (measured radiance minus modelled radiance) with the NubiScope housing temperature was found. This may be explained with rising thermal emission from the NubiScope housing with rising internal temperature, which influences the measurement. Therefore, the threshold to detect clouds was introduced as a linear function of NubiScope housing temperature. Linear regression models with the cloudless sky
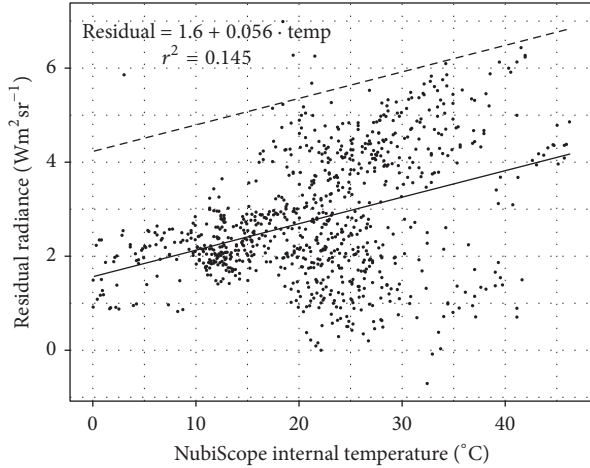
FIGURE 2: Scatterplot NubiScope internal temperature versus residual radiance (NubiScope measurement minus Streamer modelled spectral radiance) at a zenith angle of 3°. Solid line represents linear regression model of all points taken into account, dashed line is regression line plus two standard deviations of the residual radiance, and formula and r^2 belong to the regression model.

residuals as the dependent variable and the internal NubiScope temperature as independent variable were introduced for each zenith angle separately. Figure 2 shows the regression model for the 3° zenith angle case. The regression line represents the average residual versus temperature. Hence, a residual (measured minus modelled radiance) was declared cloudy, if it was more than 2 standard deviations away from the regression line. The standard deviation was calculated from all 882 cloudless sky scenes.

2.2.2. Cloud-Base Height Calculation. For cloudy pixels, the base height is calculated by assuming that the cloud droplets have the same temperature as the surrounding air and that the measured brightness temperature represents the cloud-base temperature. This temperature is compared to the respective measured atmospheric temperature profile to retrieve the cloud-base height. A linear interpolation is used to derive continuous temperature profiles from the discrete heights measured with the microwave profiler. For cloudless sky pixels, the height is derived as the average height of all valid cloud pixels to allow geolocalization of the cloudless sky area.

2.2.3. Geolocalization of the Cloud. Beyond the cloud-base temperature and height information, a sterical pixel defined by the azimuth and zenith scanning angles contains spatial information about the scanned cloud-base area. Here it was assumed that the scanned surface of a sterical pixel is a homogenous area with the form of an ellipse at a given height parallel to the ground. The form of the ellipse can be described by imagining the scanning field of view as a cone with its tip at the NubiScope and a beam angle equal to the field of view. This is illustrated in Figure 3 for a single sterical pixel with Ns as the NubiScope position.

To identify the area that lies within an ellipse, the coordinates x and y of the centre point of the ellipse as well as
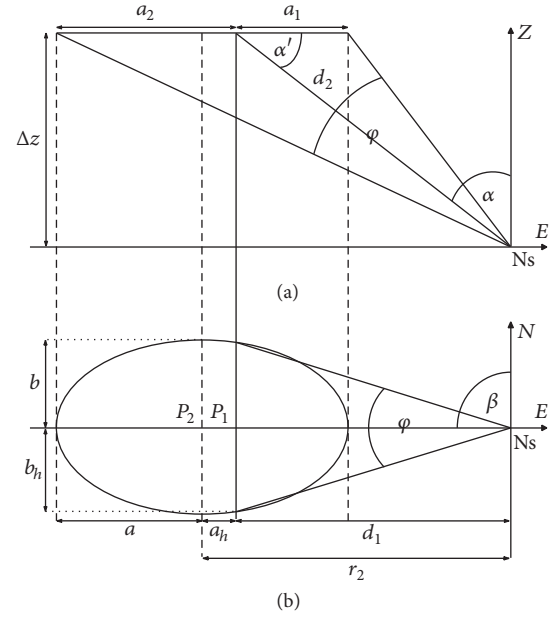

FIGURE 3: Scheme of a single measurement, (a) lateral view, (b) top view, a_i and b_i = variables concerning ellipse major and minor axis, respectively, d_i = variables concerning distance of ellipse centre point from NubiScope, α = viewing zenith angle, β = viewing azimuth angle, φ = FOV, Ns = position NubiScope, P_1 = apparent ellipse centre point, and P_2 = real ellipse centre point.

the ellipse parameters need to be calculated. Predetermined parameters are the zenith angle of the measurement α, the azimuth angle β, the field of view φ, and the cloud-base height above the ground Δz. From these parameters the distance on the ground d_1 and the direct distance d_2 from P_1 to the NubiScope Ns can be calculated.

As can be seen in Figure 3, P_1 is not the actual centre point of the ellipse but the point where the field of view axis pierces the measured ellipse. For getting the correct a, a_1 and a_2 had to be calculated first.

$$a_1 = \frac{\sin(\varphi/2)\, d_2}{\cos(\varphi/2 - \alpha)},$$

$$a_2 = \frac{\sin(\varphi/2)\, d_2}{\cos(\varphi/2 + \alpha)}, \qquad (2)$$

$$a = \frac{a_1 + a_2}{2}.$$

With the help of a, a_h, b_h, and the general ellipse equation, b can be obtained.

$$a_h = \frac{a_2 - a_1}{2},$$

$$b_h = \tan\frac{\varphi}{2}\Delta z \tan\alpha, \qquad (3)$$

$$b = \sqrt{\frac{a^2 b_h^2}{a^2 - a_h^2}}.$$

TABLE 3: Validation results for all 25 available Landsat scenes. For abbreviations refer to (5)–(7).

Zenith angle range	Number evaluated pixels	TPR	TNR	ACC	AB
0–10	10454	0.61	0.98	0.91	0.72
>10–20	21238	0.43	0.97	0.89	0.57
>20–30	31756	0.37	0.99	0.90	0.46
>30–40	81306	0.34	0.99	0.90	0.42
>40–50	145235	0.31	0.98	0.89	0.46
>50–60	247117	0.30	0.98	0.88	0.45
>60–70	1017167	0.40	0.90	0.84	1.12
>70–80	3955824	0.41	0.81	0.76	1.85

For the coordinates of the ellipse, centre point P_2 at the distance r_2 from Ns is needed instead of d_1 for P_1. This results in

$$P_1 = \begin{pmatrix} d_1 \cos \beta \\ d_1 \sin \beta \\ \Delta z \end{pmatrix},$$

$$r_2 = d_1 + a_h,$$

$$P_2 = \begin{pmatrix} r_2 \cos \beta \\ r_2 \sin \beta \\ \Delta z \end{pmatrix}. \tag{4}$$

In this way, an ellipse can be derived for each of the 1080 sterical pixels of a measurement cycle that represents the full portion of the sky which was expected to be measured. Since the geographical coordinates of the NubiScope are known, the geographical coordinates for the centre point of each ellipse can be determined.

2.3. Validation. For validation, the results of the proposed NubiScope cloud mapping algorithm were compared to the Fmask cloud mask (Section 2.1.3) derived from the Landsat scenes available during the study period (cf. Table 2). Numbers of true positive, false positive, true negative, and false negative pixels were counted within the area scanned by the NubiScope and the true positive rate (TPR; correctly identified clouds) and true negative rate (TNR; correctly identified cloudless skies) were calculated (cf. (5)). This was done separately for varying zenith angle intervals. True positive pixels are correctly identified and localized by the proposed NubiScope algorithm. False negative pixels are detected by the NubiScope algorithm, but not in the Fmask cloud mask. True negative pixels are correctly identified cloudless sky pixels and false negative pixels are wrongly classified as cloudless sky pixels.

$$TPR = \frac{\text{true positive}}{\text{true positive} + \text{false negative}},$$

$$TNR = \frac{\text{true negative}}{\text{true negative} + \text{false positive}}. \tag{5}$$

Additionally, the overall accuracy (ACC, (6)) and area bias (AB, (7)) were calculated. The ACC is the ratio of correct classifications to all classifications and has an optimum of 1. The AB shows if the total cloud area was over- (AB > 1) or underestimated (AI < 1).

$$ACC = \frac{\text{true positive} + \text{true negative}}{\text{all}}, \tag{6}$$

$$AB = \frac{\text{true positive} + \text{false positive}}{\text{true positive} + \text{false negative}}. \tag{7}$$

Concerning the calculated cloud-base height from the NubiScope data, it can be assumed to be correct if the positions of the clouds determined by the NubiScope cloud mapping algorithm and the Landsat derived cloud mask match.

Furthermore, NubiScope Cloud-Base Heights (CBH) were compared to readings from the CHM 15k ceilometer. For each NubiScope scan, the six NubiScope sterical pixels closest to zenith (1.5°) were averaged and their standard deviation was derived. The same procedure was applied to all coinciding ceilometer readings during the respective NubiScope data takes. Only NubiScope-ceilometer pairs that showed both for NubiScope and for ceilometer observations less than 50 m standard deviation were taken into account. In this way only situations with homogeneous cloud layers were considered. This filtering leads to a total number of 5737 CBH pairs for comparison. Additionally, CBH was derived with the software provided by the manufacturer for the same intervals. In the following the algorithm presented in this paper is referred to as the RTM algorithm, because it is based on radiative transfer modelling. The algorithm of the manufacturer is referred to as the IMK algorithm.

3. Results

3.1. Evaluation Statistics. Table 3 summarizes the evaluation results obtained for the 25 scenes for which Landsat and NubiScope data were available. One result was the rising number of pixels with larger zenith angles, which was caused by the extending ellipse area with increasing zenith angle. Performance analysis took place only within these ellipse areas. Altogether, the evaluation results point to a good performance of the introduced NubiScope algorithm. This holds especially true regarding the different observation geometry of the NubiScope (cloud-base) compared to Landsat (cloud-top). Despite the small number of pixels considered for the statistical analysis at small zenith angles (<10°) the TPR indicates a good performance of the proposed NubiScope
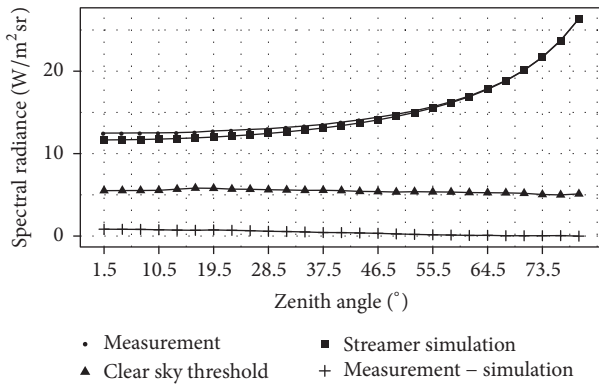
Figure 4: Measured (NubiScope) versus modelled (Streamer) radiance for different zenith angles for 16 June 2010, 09:50 UTC (residuum = measurement − simulation; cloudless sky threshold = residual radiance + 2 standard deviations).

algorithm with respect to cloud detection. At larger zenith angles cloud detection was performing less favourably but surprisingly stably. On the other hand, very high true negative rates for all zenith angles point to a better performance of the algorithm regarding the detection of cloud-free areas. This was expected, because the cloud-free decision relies on a threshold test only, whereas for correct cloud detection and localization a reliable base height assignment is required additionally to the threshold decision. Because of the higher performance in cloudless sky detection and the overall higher number of cloudless sky pixels, the accuracy was high over all zenith angle intervals with a small decreasing tendency at larger zenith angles.

Regarding area estimation, the algorithm underestimates the cloudy area up to a zenith angle of 60°. This might be explained by the cloudless sky radiance threshold. As seen in Figure 2, the threshold had to be set high to ensure that as many cloudless sky cases as possible fall below it. This increases the chance that clouds with a low emission fall under the threshold and are declared as cloudless sky. As a side effect, the overestimation of the cloud-free area might have increased the TNR, if the chosen scenes contain more cloud-free areas than cloudy areas.

3.2. Case Studies. The following section presents results of the proposed algorithm. First, a cloudless sky case is displayed to illustrate the capability of the radiative transfer modelling approach. Sections 3.2.1–3.2.4 treat case studies with varying cloud cover and cloud type.

3.2.1. Cloudless Sky on 16 June 2010. At 09:50 UTC on 16 June 2010 the sky over the MOL-RAO was cloud-free. A plot of the average measured and simulated spectral radiance per zenith angle for the NubiScope cycle can be seen in Figure 4. The residual radiance (measured radiance minus modelled radiance) ranged between −0.99 and 0.83 W m^{-2} sr^{-1}. The upper cloudless sky radiance threshold inferred for the NubiScope housing temperature of 29.5°C was 5.94 W m^{-2} sr^{-1} (see Section 2.2.1). Thus, the scene was correctly identified as cloud-free.

3.2.2. Scattered Clouds on 5 July 2011. On 5 July 2011 at 09:50 UTC, the sky over the MOL-RAO was slightly covered by cumuliform clouds, mainly in the northern and eastern part (Figures 5(a) and 5(b)). The ellipses assigned by the NubiScope algorithm resembled the overall Fmask-based cloud distribution (Figure 5(b)) with cloudless sky over the MOL-RAO and a ring of broken clouds in the near surroundings up to a distance of ~2.5 km. Apart from some single false positive detection instances, the cloudless sky corridor running from the northwestern to the southeastern part was detected correctly (Figure 5(b)). Altogether, despite a general underestimation of the cloud cover (AB of 0.74), the cloudy area was somewhat overestimated by the NubiScope algorithm at larger zenith angles. This might be due to misplaced scattered clouds and cloud edges that did not fully cover the sterical pixels. Because of the cloud signal within the pixels, they were correctly declared as cloudy. However, because of the cloudless sky signal within the scanned FOV the measured brightness temperature is reduced leading to a too high height assignment and as a consequence to a wrong geolocalization. This effect led to an overall low true positive rate (zenith angles < 80°) of 0.31. However, the overall true negative rate was high with 0.90. The overall accuracy was 0.78.

3.2.3. Dense Clouds on 19 June 2011. On 19 June 2011 at 09:50 UTC, a bulk of dense clouds covered the sky over the MOL-RAO, extending from the southwest to the Northeast (Figure 6). In the Northeast, the cloud area dissolved into translucent clouds. Altogether, the NubiScope algorithm reproduced the Fmask cloud pattern quite well. Ellipses in the southern and northeastern part appeared to be compressed in distance and extended only up to ~2.5 km. This was because the dense cover with optically thick clouds prevented measurements at greater distances even at large zenith angles. The dense cover also stimulated a high TPR of 0.74. The few ellipses in the East and Southeast at distances of up to 7.5 km from the MOL-RAO were due to cloud gaps allowing measurements from greater distances. Over the optically thin clouds in the Northwest, calculated cloud bases were higher. However, classification accuracy in this area was lower. Overall TNR was low with 0.76 compared to the average performance (Table 2). This resulted from misclassifications due to mixed signals in the Northwest. Overall accuracy of 0.75 was high compared to average performance. The AB of 0.78 denotes underestimation of cloudy area. This was mainly caused by large ellipses that were false negative.

3.2.4. Translucent Clouds on 29 August 2011. On 29 August 2011 at 09:56 UTC, the sky over the MOL-RAO was dominated by optically thin clouds from the Southwest to the Northeast (Figure 7). As can be seen in Figure 7(b), the NubiScope algorithm detected cloudy and cloud-free areas in good accordance with the Fmask algorithm. The overall TPR (zenith angle < 80°) was 0.78, TNR was 0.74, and accuracy was 0.75. Moreover, the NubiScope algorithm correctly differentiated between the lower cloud-base heights of the optically denser cumuliform cloud layers at a distance of up to ~3 km and the higher cloud-base heights of the more translucent
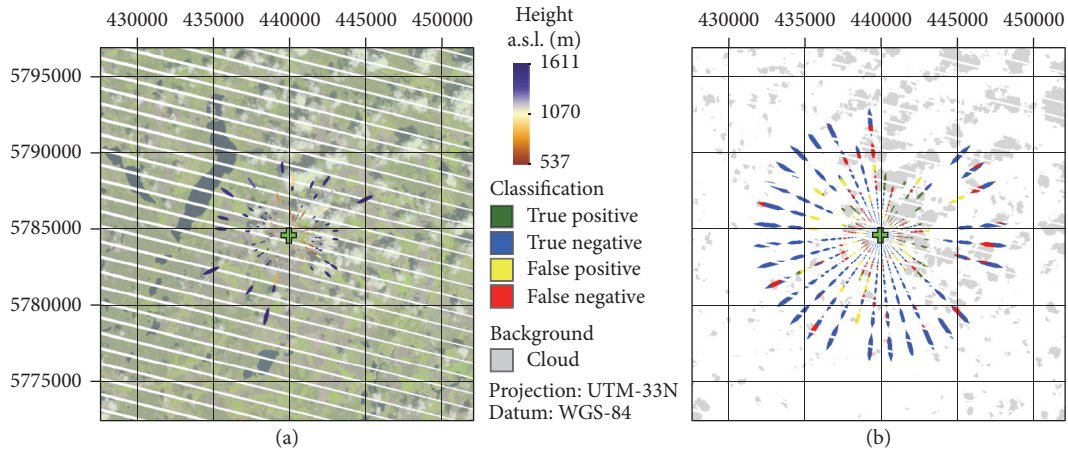
FIGURE 5: (a) Evaluation for 5 July 2011, 09:50 UTC. Ellipse colours represent height, ETM+ true-colour composite as background image. The position of the NubiScope is marked with a green cross. Only ellipses which passed the cloud test are presented; cloudless sky ellipses are not shown. (b) Evaluation of classifications with Fmask as reference. For the purpose of visualization, the cloud ellipses detected by the NubiScope overlay the Landsat images.
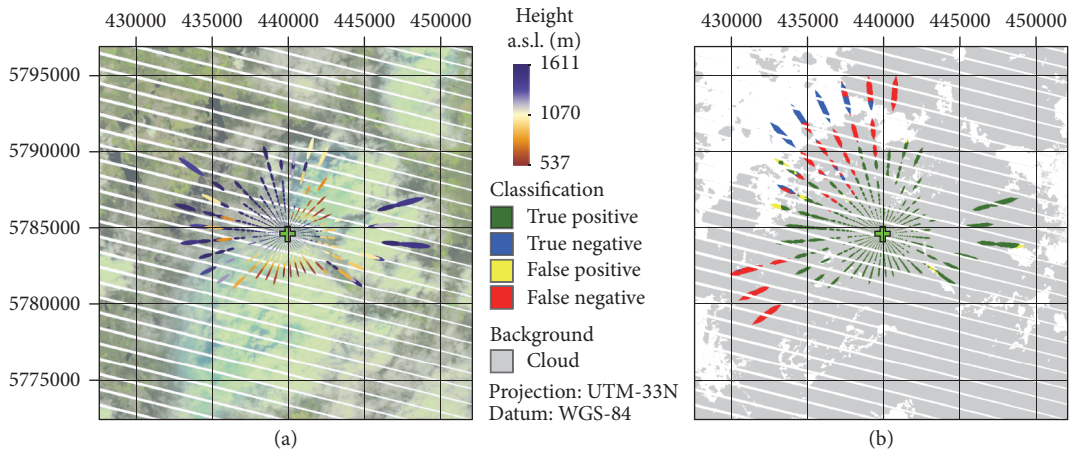

FIGURE 6: As Figure 5, but for 19 June 2011 09:50 UTC.

cloud layer at a greater distance of more than 5 km from the MOL-RAO. The two cloud layers are also visible in the Landsat RGB image and are reproduced by the calculated heights of the respective ellipses (Figure 7(a)). Problems are obvious for the few clouds in the northwestern parts. The four cloudy ellipses detected by the algorithm hardly match the real clouds. This misclassification is due to the extending area of the ellipses at larger zenith angles. Since the small clouds do not cover the ellipse area completely, the measured radiance consists of a cloudy and a cloudless sky background signal. The sterical pixels were identified correctly as cloudy because the measured radiation was too high for cloudless sky. However, the cloud's temperature cannot be determined correctly. This results in lower brightness temperatures and finally higher cloud-base estimations. These oversized ellipses also contributed to an overestimation of the cloudy area (AB of 1.02).

3.3. Cloud-Base Height. The NubiScope CBH based on the RTM algorithm agreed differently with ceilometer CBH on different heights (Figure 8(a)). Below 4000 m the RTM algorithm underestimated CBH by 302 m compared to the ceilometer. Above 4000 m NubiScope RTM estimated CBH on average 1647 m lower. In case of high clouds NubiScope CBH appeared to be largely independent of the ceilometer CBH. This could stem from the pertinent effect of atmospheric emission which leads to underestimation of CBH. Comparable to these results the IMK algorithm underestimated CBH below 4000 m compared to the ceilometer by 390 m and above 4000 m by 1013 m. However, in 1520 cases the algorithm delivered no results. According to Wauben et al. (2012) this happens when total cloud cover is below 12.5%.

4. Discussion

The proposed RTM based algorithm showed good capabilities to detect sterical pixels of cloudless sky. This is supported by the overall performance concerning cloudless sky detection as well as by the cloudless sky case study. The
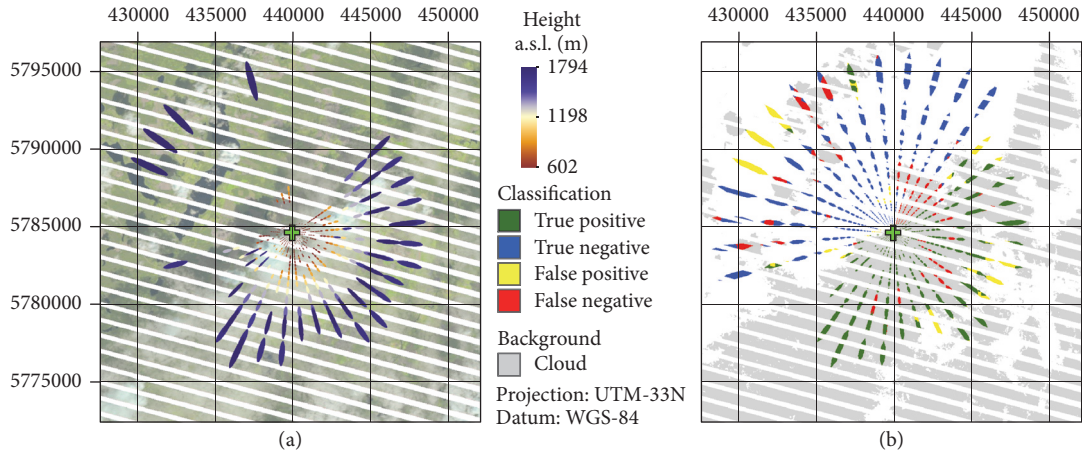
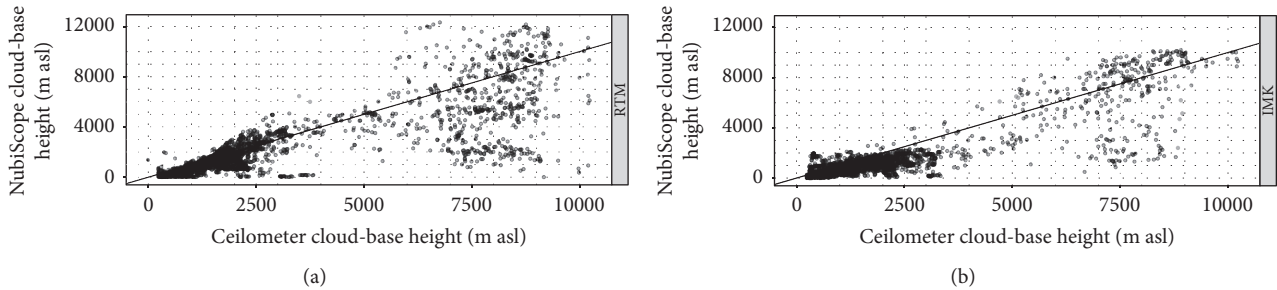FIGURE 7: As Figure 5, but for 29 August 2011, 09:56 UTC.

FIGURE 8: Comparison of cloud-base height derived by ceilometer and NubiScope. Two panels refer to CBH derived with algorithm presented in this study (RTM, (a)) and manufacturer's algorithm (IMK, (b)). Solid diagonal lines represent 1:1 lines.

spatial extents of cloudless sky regions are depicted in high accordance with the Fmask results.

For the detection of cloudy sterical pixels, a lower performance has to be stated. The presented case studies provide some explanations for these results. The presented algorithm assumes clouds to fit neatly into the sterical pixels. This leads to problems for cloud edges and small clouds. As the measured signal consists of both cloud and cloudless sky background, it is identified as cloudy, because its radiation is higher than cloudless sky radiation. However, the cloud's temperature cannot be determined correctly, which results in a lower brightness temperature and finally higher cloud-base estimation. Smaller viewing angles of the NubiScope and the restriction to lower smaller zenith angles might improve the classification results.

The correct mapping of translucent and broken clouds is complicated by the same effect. The mixed cloudy and cloudless sky signal in the respective sterical pixel decreases the measured radiance (e.g., [20]) and leads to a reduced brightness temperature compared to an opaque cloud with the same cloud-base temperature and base height. This effect cannot be counteracted by decreasing the instruments FOV, but it requires more information on the cloud type and its emissivity. The same mechanism hinders the correct mapping of translucent clouds such as cirrus. As cirrus clouds are usually not opaque and let the background sky transmit, they have reduced T_b compared to an opaque cloud at the same

height and temperature. These cloudless sky regions reduce the measured radiance (e.g., [20]). Again more information about the cloud type would be required. Additionally, a sterical pixel might represent the side of a cloud, instead of its base. As higher parts of the clouds generally have lower temperatures, the cloud base will be mapped on a lower height.

Another problem is due to the radiometry itself. The radiative transfer model Streamer is used to estimate cloud-free atmospheric radiation. For cloudy cases, the cloud's base height determines how much of the cloud-free atmospheric path is part of the measured signal. Thurairajah and Shaw [17] argue that subtracting the whole atmospheric emission from the signal "is a self-correcting problem for cloud detection since high clouds are above essentially all of the water vapour and thick clouds are easy to detect because of their large residual radiance." If the goal is to determine the cloud's own emission, not only detecting it, this statement is still true for high clouds. However, low clouds shield higher parts of the atmosphere that might still have substantial emission. In this case subtracting the whole of the atmosphere's emission from the signal leads to underestimation of the cloud's emission. Therefore, eliminating the atmospheric emission from the measured signal remains an open issue. A solution for this could be to use model inversion approaches: one has to insert clouds into the RTM simulations and then use empirical fitting methods to iteratively minimize a cost function based

on the cloud parameters and the IR observations. Emulators of the radiative transfer model built with machine learning techniques could help to speed up the optimisation procedure and allow operational processing [21]. The spatial pattern of the measured T_b could help to identify the number of clouds layers and the algorithm described here to give initial estimates for the CBH. Furthermore, such an approach of full radiative transfer model inversions can take the cloud's reflection of terrestrial thermal emission into account, although this is only a few percent in the thermal infrared [22].

In summary, the violation of the assumption of the cloud filling a sterical pixel completely, the assumption of opaque clouds, and the assumption of viewing the cloud base generally lead to an overestimation of CBH, while the neglecting of atmospheric thermal emission and the cloud's reflection of thermal emission lead to an underestimation.

The different viewing geometries between the NubiScope, which scans the cloud base, and the Landsat sensor scanning the cloud top hinder a proper evaluation of the proposed NubiScope algorithm. Area-wide information about the cloud-base height (e.g., from scanning cloud radar or lidar) would allow determining potential problems more precisely and help to improve the introduced algorithm.

5. Conclusions

Clouds are highly dynamic atmospheric phenomena in space and time. They strongly influence the Earth's radiation budget by shielding the Earth from incoming shortwave radiation and reducing outgoing longwave radiation. On a global mean basis, they have a net cooling effect with a rate of around $-20\,\mathrm{W\,m^{-2}}$ [23]. However, their local effects depend on their highly variable micro- and macrophysical properties. In this context, ground-based remote sensing systems have the capability to observe local cloud distribution with a high spatiotemporal resolution.

In this study, it was shown that the IR imager NubiScope has the potential for day-and-night observation of clouds. The system allows spatial cloud mapping with a high spatiotemporal resolution. For this purpose, an algorithm is proposed which detects cloudless sky and cloudy pixels in a first step by comparing the measured signal with a simulated cloudless sky signal for the respective atmospheric temperature and water vapour profile. Based on the current atmospheric profile the measured cloud-base temperature is converted into CBH. The calculated base height is used in combination with the viewing geometry to geolocate the observed cloud.

This approach is different from the IMK algorithm, which uses static lapse rates and gives cloud cover in different layers, but without explicit spatial locations. The spatial information can be used in cases where the cloud location has additional importance, for instance, at transition zones between cloud regimes. It also allows a more straightforward comparison to satellite imagery as demonstrated in this study.

The performance of the algorithm was evaluated by means of Landsat Fmask cloud masks and true-colour images. The results showed general agreement between the patterns produced by the algorithm and Landsat Fmask. Best results were obtained for cumulus clouds with a maximal

distance of 5 km from the NubiScope. Furthermore, cloudless sky areas were recognized with high accuracy at various zenith angles. More problems occurred with translucent optically thin clouds and at greater distances, that is, at larger zenith angles. In comparison with the IMK algorithm, the RTM approach was able to slightly improve CBH retrievals when compared to a ceilometer for clouds lower than ~4 km. Higher clouds presented problems for both algorithms.

Future studies should address the ambiguity problem of mixed pixels. Including a cloud model in the radiative transfer modelling can serve as a model inversion technique in contrast to the simple threshold used here. The spatial patterns of measured brightness temperatures might contain information about the cloud type at hand, which can support the radiative transfer modelling. On the other hand, cloud climatologies could be created based on the proposed algorithm and compared to other climatologies to investigate the performance over longer time spans. Furthermore, thorough sensitivity analysis of all algorithm input parameters, including the cloud/no-cloud decision rule, pyrometer, and atmospheric profiler errors, should be performed. This will help to focus efforts to improve the algorithm's performance.

Conflicts of Interest

The authors declare no conflicts of interest regarding the publication of this article.
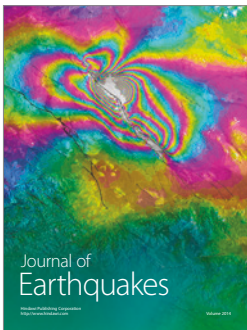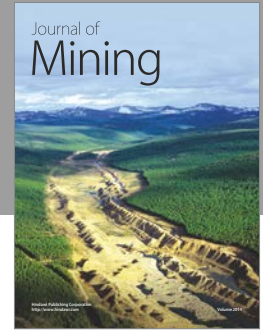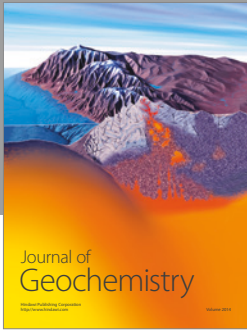
Acknowledgments

References

[1] Intergovernmental Panel on Climate Change, *Climate Change 2013: The Physical Science Basis. Contribution of Working Group I to the Fifth Assessment Report of the Intergovernmental Panel on Climate Change*, T. F. Stocker, D. Qin, G.-K. Plattner, Eds., Cambridge University Press, Cambridge, UK, 2013.

[2] J. Bendix, R. Rollenbeck, and W. E. Palacios, "Cloud detection in the tropics-a suitable tool for climate - ecological studies in the high mountains of Ecuador," *International Journal of Remote Sensing*, vol. 25, no. 21, pp. 4521–4540, 2004.

[3] C. Merk, J. Cermak, and J. Bendix, "Retrieval of optical and microphysical cloud properties from Meteosat SEVIRI data at night - a feasibility study based on radiative transfer calculations," *Remote Sensing Letters*, vol. 2, no. 4, pp. 357–366, 2011.

[4] R. Tapakis and A. G. Charalambides, "Equipment and methodologies for cloud detection and classification: a review," *Solar Energy*, vol. 95, pp. 392–430, 2013.

[5] J. E. Shields, M. E. Karr, R. W. Johnson, and A. R. Burden, "Day/night whole sky imagers for 24-h cloud and sky assessment: history and overview," *Applied Optics*, vol. 52, no. 8, pp. 1605–1616, 2013.

[6] P. W. Nugent, J. A. Shaw, N. J. Pust, and S. Piazzolla, "Correcting calibrated infrared sky imagery for the effect of an infrared window," *Journal of Atmospheric and Oceanic Technology*, vol. 26, no. 11, pp. 2403–2412, 2009.

[7] H. M and T. Sattler, "NubiScope," http://nubiscope.de, 2015.

[8] W. Wauben, "Evaluation of the NubiScope," KNMI Technical Report No 291, De Bilt, Netherlands, 2006, http://bibliotheek.knmi.nl/knmipubTR/TR291.pdf.

[9] W. Wauben, F. Bosveld, and H. K. Baltink, "Laboratory and field evaluation of the Nubiscope," *WMO TECO, Helsinki*, 2010.

[10] R. Boers, M. J. De Haij, W. M. F. Wauben et al., "Optimized fractional cloudiness determination from five ground-based remote sensing techniques," *Journal of Geophysical Research: Atmospheres*, vol. 115, no. 24, pp. 1–16, 2010.

[11] U. Feister, H. Möller, T. Sattler, J. Shields, U. Görsdorf, and J. Güldner, "Comparison of macroscopic cloud data from ground-based measurements using VIS/NIR and IR instruments at Lindenberg, Germany," *Atmospheric Research*, vol. 96, no. 2-3, pp. 395–407, 2010.

[12] *Meteorologisches Observatorium Lindenberg - Richard-Aßmann-Observatorium*, Deutscher Wetterdienst, Germany, 2012, http://www.dwd.de/mol.

[13] M. A. Janssen, "An introduction to the passive remote sensing of atmospheres , in atmospheric remote sensing by microwave," in *Atmospheric Remote Sensing by Microwave Radiometry*, M. A. Janssen, Ed., pp. 1–36, J. Wiley & Sons, Inc, New York, NY, USA, 1993.

[14] E. R. Westwater, S. Crewell, C. Mätzler, and D. Cimini, "Principles of surface-based microwave and millimeter wave radiometric remote sensing of the troposphere," *Proceedings of the Italian Society of Electromagnetics SIEM*, vol. 1, no. 3, pp. 50–90, 2005.

[15] S. Crewell, U. Löhnert, M. Mech, and C. Simmer, "Mikrowellenradiometrie für Wasserdampf- und Wolkenbeobachtung," *promet*, vol. 36, no. 3-4, pp. 109–118, 2010.

[16] Z. Zhu and C. E. Woodcock, "Object-based cloud and cloud shadow detection in Landsat imagery," *Remote Sensing of Environment*, vol. 118, pp. 83–94, 2012.

[17] B. Thurairajah and J. A. Shaw, "Cloud statistics measured with the Infrared Cloud Imager (ICI)," *IEEE Transactions on Geoscience and Remote Sensing*, vol. 43, no. 9, pp. 2000–2007, 2005.

[18] J. R. Key and A. J. Schweiger, "Tools for atmospheric radiative transfer: streamer and fluxnet," *Computers and Geosciences*, vol. 24, no. 5, pp. 443–451, 1998.

[19] R. G. Ellingson, J. Ellis, and S. Fels, "The intercomparison of radiation codes used in climate models: long wave results," *Journal of Geophysical Research: Atmospheres*, vol. 96, no. 5, pp. 8929–8953, 1991.

[20] J.-C. Dupont, M. Haeffelin, and C. N. Long, "Evaluation of cloudless-sky periods detected by shortwave and longwave algorithms using lidar measurements," *Geophysical Research Letters*, vol. 35, no. 10, Article ID L10815, 2008.

[21] J. Verrelst, N. Sabater, J. P. Rivera et al., "Emulation of leaf, canopy and atmosphere radiative transfer models for fast global sensitivity analysis," *Remote Sensing*, vol. 8, no. 8, article no. 673, 2016.

[22] G. Yamamoto, M. Tanaka, and S. Asano, "Radiative transfer in water clouds in the infrared region," *Journal of the Atmospheric Sciences*, vol. 27, no. 2, pp. 282–292, 1970.

[23] P. E. Ardanuy, L. L. Stowe, A. Gruber, and M. Weiss, "Shortwave, longwave, and net cloud-radiative forcing as determined from Nimbus 7 observations," *Journal of Geophysical Research: Atmospheres*, vol. 96, no. D10, p. 18537, 1991.